

# A Galactic breeze origin for the Fermi bubbles emission

Olivier Tourmente<sup>1\*</sup>, D. Rodgers-Lee<sup>2,3</sup> and Andrew M. Taylor<sup>1</sup>

<sup>1</sup>*Deutsches Elektronen-Synchrotron, Zeuthen, Germany*

<sup>2</sup>*School of Cosmic Physics, Dublin Institute for Advanced Studies, 31 Fitzwilliam Place, D02 XF86, Ireland*

<sup>3</sup>*School of Physics, Trinity College Dublin, University of Dublin, College Green, Dublin 2, D02 PN40, Ireland*

Accepted XXX. Received YYY; in original form ZZZ

## ABSTRACT

The origin of the Fermi bubbles, which constitute two gamma-ray emitting lobes above and below the Galactic plane, remains unclear. The possibility that this Fermi bubbles gamma-ray emission originates from hadronic cosmic rays advected by a subsonic Galactic outflow, or breeze, is here explored. The simulation of a breeze solution and subsequent cosmic ray transport is carried out using the hydrodynamical code, PLUTO, in combination with a cosmic ray transport code. The Galactic outflow model obtained is found to be compatible with both inferences of the decelerating outflow velocity profile of the gas in the Fermi bubbles region, and evidence for the presence of a large amount of hot ionised gas out in the Galactic halo region. Although simple, this model is found to be able to reproduce the observed Fermi-LAT energy flux at high Galactic latitudes. Following these results a prediction concerning the gamma-ray emission for 1-3 TeV photons is made for future comparison with CTA/SWGO measurements.

**Key words:** Galaxy: halo – gamma-rays: galaxies – cosmic rays – ISM: jets and outflows

## 1 INTRODUCTION

Observations and measurements have provided evidence of outflows in galactic centers (GCs) for several decades (Lynds & Sandage 1963; Burbidge et al. 1964; Mathews & Baker 1971; Songaila 1997). Such outflows have also been observed from the Milky-Way in a broad energy range from radio (Lockman 1984) to X-ray (Morris & Serabyn 1996; Cheng et al. 1997).

A decade ago, two Galactic bubbles lobes extending above and below the GC were first detected with the Fermi-LAT instrument in the gamma-ray energy band (Su et al. 2010; Dobler et al. 2010). The extension of this emission is  $\sim 50^\circ$  in Galactic latitude and  $\sim 40^\circ$  in Galactic longitude. Furthermore, the spectral energy distribution of this gamma-ray emission is rather hard, exhibiting a spectral downturn or cut-off at an energy of  $\sim 300$  GeV (Ackermann et al. 2014). The brightness intensity of this emission appears approximately constant within the bubbles, with a sudden sharp edge feature observed at their boundary (Ackermann et al. 2014). Those gamma-ray bubbles are potentially a counterpart of the microwave haze (Finkbeiner 2004; Planck Collaboration et al. 2013), with both exhibiting hard spectra. In the X-ray band, recent observations of larger scale eROSITA bubbles, which appear to enshroud the Fermi bubbles, are likely connected to the Fermi bubbles structures (Predehl et al. 2020).

Despite the wealth of observational data, there remains no clear consensus about the underlying mechanism that pro-

duces the outflow responsible for the formation of those bubbles. Three features must be fully explained to give a satisfying theory (Yang et al. 2018). These are related to the emission mechanism, the location of the event and the acceleration mechanism of the cosmic rays (CRs) that are responsible for the gamma-ray emission. Considering the hard spectrum of the Fermi bubbles, the emission may be generated by hadronic CR energy losses. In such scenarios, hadronic CRs are transported via starburst or active galactic nucleus winds (Crocker & Aharonian 2011; Mou et al. 2014; Crocker et al. 2015; Mou et al. 2015). The wind velocities in these models range from a few hundred of  $\text{km s}^{-1}$  to a few thousand of  $\text{km s}^{-1}$  and the timescale for the bubbles to be formed is between  $\sim 10$  Myr to 1 Gyr.

Alternatively, the Fermi bubbles emission could also be produced by leptonic CR energy losses, with such leptons first being transported via an active galactic nucleus jet (Guo & Mathews 2012; Yang et al. 2012, 2013; Yang & Ruszkowski 2017; Guo 2017). For these models, the short cooling time of electrons implies that the age of the Fermi bubbles should be no more than a few Myr. Alternatively, these CR leptons may be accelerated near the gamma-ray production site (Cheng et al. 2011; Sarkar et al. 2017; Mertsch & Petrosian 2019).

Even if the hadronic wind models exhibit a much lower velocity than the leptonic jet models the majority of proposed models assume a supersonic velocity above  $\sim 500$   $\text{km s}^{-1}$ . However, UV absorption line observations of cold clouds in the Fermi bubbles, from low to high Galactic latitudes, show velocities ranging from  $\sim 100 - 300$   $\text{km s}^{-1}$  and with a continuous deceleration (Fox et al. 2015; Bordoloi et al. 2017;

\* E-mail: olivier.asin@desy.de

Karim et al. 2018; Lockman et al. 2020; Ashley et al. 2020; Cashman et al. 2021; Sofue 2022). This last feature contradicts the supersonic wind model for which a shock should be seen producing strong perturbations in the velocity profile and in the ambient density.

Small Galactic outflow velocities are consistent with expectations for a thermally driven outflow (Parker 1958, 1965; Chamberlain 1965). This model is motivated from considerations of the momentum transport equation, which provides two possible solutions, a transonic and a subsonic one. The transonic description has previously been applied in galactic outflow models (Holzer & Axford 1970; Chevalier & Clegg 1985; Everett & Murray 2007) and galactic fountain models (de Avillez & Breitschwerdt 2004; Bustard et al. 2018; Chan et al. 2021). The subsonic description is less explored, with only stability analysis of such outflows having been made (Fichtner 1997).

Following the first UV absorption line observations of cold clouds expanding in the Fermi bubbles, Taylor & Giacinti (2017) proposed an alternative where CRs are both diffused and advected within a Galactic breeze. The subsonic profile that Taylor & Giacinti (2017) used was expressed as an analytic, divergence-free outflow velocity profile. This outflow with pre-accelerated hadronic CRs at its base was launched from the GC, subsequently producing  $\gamma$ -ray emission via proton-proton interactions with the diffuse ambient gas out in the halo region. In this work, the model is investigated further by relaxing the divergence-free assumption for the subsonic outflow by using a hydrodynamics code. The velocity profile thus produced is used in the CR transport code, taking into account advective processes. The model is a first step to study the feasibility of a Galactic breeze solution for reproducing the Fermi bubbles emission. Therefore, a single isothermal Galactic gas temperature has been assumed and the model does not include a magnetic field but instead adopts a single homogeneous diffusion coefficient.

The paper is structured as follows: in section 2 the Galactic hydrodynamical model and the gravitational potential are introduced, as well as the numerical setup. Section 3 described the transport equation for hadronic CRs and the computational grid. The subsequent results are presented in section 4 and the conclusions and outlook are given in section 5.

## 2 GALACTIC OUTFLOW MODEL

To simulate the launching region and propagation of an outflow into the Galactic halo region, a hydrodynamic description has been simulated using the PLUTO code (Mignone et al. 2007). This numerical scheme solves the mass and momentum conservation equations throughout the computational grid domain,

$$\frac{\partial \rho}{\partial t} + \nabla \cdot (\rho \mathbf{v}) = S_\rho, \quad (1)$$

$$\frac{\partial}{\partial t}(\rho \mathbf{v}) + \nabla \cdot (\rho \mathbf{v} \mathbf{v} + p \mathbf{I}) = -\rho \nabla \Phi_{\text{eff}}. \quad (2)$$

In these expressions,  $\rho$ ,  $\mathbf{v}$  and  $p$  are the mass density, velocity and thermal pressure of the gas in the Galaxy, respectively.  $\mathbf{I}$  is the unitary tensor. The term  $S_\rho$  represents the injected mass and  $\Phi_{\text{eff}}$  is the effective gravitational potential (see section 2.1.4) determined by first calculating the total

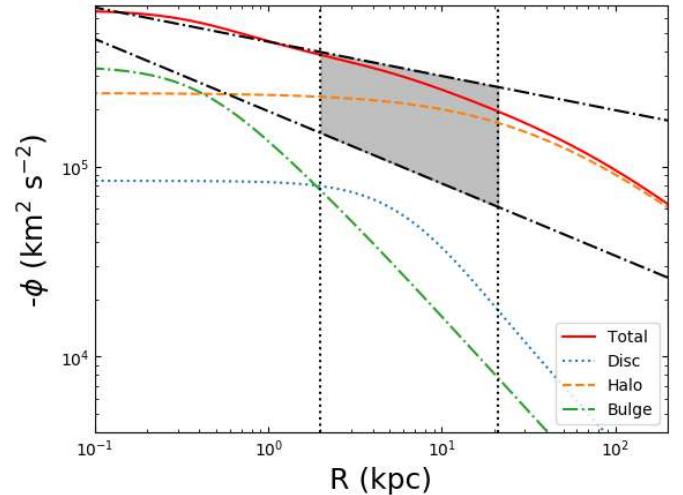


**Figure 1.** Determination of the total gravitational potential of the Milky Way (solid red line) based on observations from the Gaia mission (Watkins et al. 2019). The total potential is composed of a bulge (dot-dashed green line), disc (dotted blue line) and dark matter halo component (dashed orange line). The two vertical dotted black lines at  $R = 2$  and  $21$  kpc indicate the spatial range for which the inferred Gaia constraint is applicable. The dot-dashed black lines show the extent of the best-fitting power laws from the Gaia observations in the  $2$ - $21$  kpc region and their extension beyond this range.

gravitational potential,  $\Phi$ . Since an isothermal gas temperature is adopted (see section 2.3), here the energy conservation equation has been omitted. Details about the computational grid are provided in section 2.3. It should be noted that the effect of the presence of CRs is not included in the hydrodynamical simulation, with the CRs assumed to have no dynamical effect. Following our simulation calculations, for all simulation time steps, the thermal pressure is found to be superior to the CR pressure throughout the simulation grid, except at the injection site where the CR pressure is higher by a factor of  $\sim 1.8$ .

### 2.1 Galactic gravitational potential

The total Galactic gravitational potential,  $\Phi$ , results from the sum of three components, a bulge ( $\Phi_b$ ), disc ( $\Phi_d$ ), and dark matter halo ( $\Phi_{\text{DM}}$ ) such that

$$\Phi = \Phi_b + \Phi_d + \Phi_{\text{DM}}. \quad (3)$$

The Gaia mission (Gaia Collaboration et al. 2016a,b, 2018) has provided proper motions for approximately one billion stars. With these new data a range of power-laws have been provided for fitting the Milky Way’s gravitational potential (Watkins et al. 2019) giving a constraint for simulations. In figure 1 those fitting power-laws (dot-dashed black lines) have been compared with  $\Phi$  (solid red line) used for the simulations here. Next, we describe each component of the gravitational potential.

### 2.1.1 The bulge potential

The central bulge potential (dot-dashed green line in figure 1),  $\Phi_b$ , is based on [Flynn et al. \(1996\)](#) and is described by

$$\Phi_b = \sum_{i=1}^2 -\frac{GM_{C_i}}{\sqrt{r^2 + r_{C_i}^2}}, \quad (4)$$

where  $r$  is the spherical radius and  $M_{C_1}$ ,  $M_{C_2}$ ,  $r_{C_1}$  and  $r_{C_2}$  are given in table 1.

### 2.1.2 The disc potential

The disc potential (dotted blue line in figure 1),  $\Phi_d$ , is based on [Flynn et al. \(1996\)](#) which is a three component Miyamoto-Nagai potential ([Miyamoto & Nagai 1975](#)) given by

$$\Phi_d = \sum_{i=1}^3 -\frac{GM_{D_i}}{\sqrt{R^2 + (a_i + \sqrt{z^2 + b^2})^2}}, \quad (5)$$

where  $R$  and  $z$  are the cylindrical coordinates and  $M_{D_1}$ ,  $M_{D_2}$ ,  $M_{D_3}$ ,  $a_1$ ,  $a_2$ ,  $a_3$  and  $b$  are given in table 1.

### 2.1.3 The dark matter halo potential

The dark matter halo potential (dashed orange line in figure 1),  $\Phi_{DM}$ , is given by a Navarro-Frenk-White (NFW) profile ([Navarro et al. 1996](#)),

$$\Phi_{DM} = -\frac{GM_{200}}{r_s f(c_{200})} \frac{\ln(1 + r/r_s)}{r/r_s}, \quad (6)$$

where the function  $f(c_{200}) = \ln(1 + c_{200}) - c_{200}/(1 + c_{200})$ ,  $M_{200} = 2 \times 10^{12} M_\odot$  ([Taylor et al. 2016](#)) and  $c_{200}$  is the concentration parameter defined as  $c_{200} = r_{200}/r_s$  where  $r_{200} = 258$  kpc and  $r_s = 21.5$  kpc is the scale radius.

### 2.1.4 The effective Galactic potential

Observations of the Milky Way's rotation curve within the disc indicate velocities of  $\sim 200$  km s<sup>-1</sup> beyond 2 kpc from the GC ([Sofue 2013](#); [Bhattacharjee et al. 2014](#)). Eqs. (1) and (2) have then been solved in a rotating frame since such a Galactic rotational velocity value cannot be neglected for a Galactic breeze model, for which the outflow velocity is similar in magnitude to the Galactic rotation velocity. In the rotating frame, the effective Galactic potential,  $\Phi_{\text{eff}}$ , used in Eq. (2) is of the form,

$$\Phi_{\text{eff}} = \Phi + \frac{R}{2} \left( \frac{d\Phi}{dR} \right). \quad (7)$$

## 2.2 1D spherical Galactic outflow

Some intuition on the outflow evolution can be found through the consideration of a 1D spherically symmetric outflow ([Parker 1958, 1965](#); [Chamberlain 1965](#); [Lamers & Cassinelli 1999](#)). For this case, mass flux conservation leads to the relation

$$\dot{M} = 4\pi r^2 \rho(r) v(r), \quad (8)$$

Component	Parameter	Value
$\Phi_b$	$r_{C_1}$	2.7 kpc
	$M_{C_1}$	$6.0 \times 10^9 M_\odot$
	$r_{C_2}$	0.42 kpc
	$M_{C_2}$	$3.2 \times 10^{10} M_\odot$
$\Phi_d$	$b$	0.3 kpc
	$a_1$	5.81 kpc
	$M_{D_1}$	$1.32 \times 10^{11} M_\odot$
	$a_2$	17.43 kpc
	$M_{D_2}$	$-5.8 \times 10^{10} M_\odot$
	$a_3$	34.86 kpc
$M_{D_3}$	$6.6 \times 10^9 M_\odot$	
$\Phi_{DM}$	$r_s$	21.5 kpc

**Table 1.** List of parameters for the Galactic gravitational potential model.

where  $\dot{M}$  is defined as the mass loss rate. The momentum flux conservation equation, assuming an isothermal, steady-state evolution, leads to the relation

$$v \frac{dv}{dr} + \frac{c_s^2}{\rho} \frac{d\rho}{dr} + \frac{d\Phi}{dr} = 0, \quad (9)$$

where  $c_s$  is the thermal velocity. By differentiating Eq. (1) to get the density gradient and substituting it into Eq. (2) the following expression is obtained

$$\frac{1}{v} \frac{dv}{dr} = \frac{1}{r} \left( \frac{2c_s^2 - r \frac{d\Phi}{dr}}{v^2 - c_s^2} \right). \quad (10)$$

The numerator on the right-hand side of this expression goes to zero when  $r \frac{d\Phi}{dr} = 2c_s^2$ . The radius where this occurs is called the critical radius,  $r_c$ . Beyond  $r_c$ , for a positive numerator, a transonic outflow will accelerate while a subsonic outflow will decelerate. The behavior of a transonic outflow and its different solutions have been studied in a gravitational potential of a cold dark matter halo ([Tsuchiya et al. 2013](#); [Igarashi et al. 2014, 2017](#)). Moreover a transonic outflow considerably reduces the ambient density whereas a subsonic outflow does not. These effects are described in greater detail in appendix A.

The total effective potential model adopted for the Galaxy is not entirely spherically symmetric due to both the disc component and the Galactic rotation. These effects have an influence on the determination of the value of  $r_c$ . This value is important since it determines the subsequent velocity evolution which is discussed in the following section.

## 2.3 Galactic gas temperature and density profile

As discussed at the beginning of section 2, the hydrodynamic equations (see Eq. (1) and (2)) are considered for an isothermal gas. Indeed, observations of the Galactic halo gas do not show strong temperature fluctuations ([Tumlinson et al. 2017](#)).

Based on [Watkins et al. \(2019\)](#), the normalisation for the Galactic potential,  $\Phi$ , has been adopted with a value at the upper end of the allowed range (see Fig. 1 and section 2.1). In order to maximise the outflow velocity, while maintaining the existence of  $r_c$  beyond the radius where the CRs are injected, a gas temperature of  $kT \approx 400$  eV (ie.  $c_s \approx 250$  km s<sup>-1</sup>)

is adopted. By choosing these values for  $\Phi$  and  $c_s$  implies  $r_c \approx 1$  kpc (see section 2.2). This value of  $kT \approx 400$  eV is compatible with recent observations of the Galactic halo that presents a mixed hot-warm phase with a hot phase for which the temperature can reach  $\sim 1$  keV (Das et al. 2021). It should be noted that a small increase in the gas temperature does not significantly change the critical radius and thus has little effect on the results.

For the initial gas density setup, a hydrostatic density distribution is assumed, dictated by the Galactic potential,  $\Phi$ , and the single gas temperature with thermal velocity,  $c_s$ . This initial spatial gas number density distribution can be expressed as,

$$n_{\text{halo}} = n_{10\text{kpc}} \exp\left(-\frac{\Phi}{c_s^2}\right), \quad (11)$$

where  $n_{10\text{kpc}}$  is a normalisation constant. Its value has been fixed at  $n_{10\text{kpc}} = 10^{-3} \text{ cm}^{-3}$  in order to be compatible with the observational values provided in a range of 10-100 kpc (Gupta et al. 2017; Martynenko 2022). Fig.A1 in Appendix A shows the hydrostatic gas number density distribution adopted in this paper.

## 2.4 Numerical setup

As shown in section 2.2, Eq. (10) implies that an outflow driven by thermal gas pressure can reach a given velocity at  $r_c$  for a particular velocity  $v_0$  at the launching zone  $r_0$ . For the simulations, the combination of values adopted for  $v_0$  and the thermal temperature collectively dictate the maximum velocity of the outflow at the critical radius,  $r_c$ . Although a subsonic solution at  $r_c$  only requires the outflow to reach a Mach number  $M < 1$ , for our simulations the outflow reaches  $M = 0.85$  at  $r_c$ . The inner radius,  $r_0$ , is fixed to be  $r_0 = 300$  pc. The thermal pressure at  $r_0$  is then defined as  $P_0 = \rho_0 c_s^2$ . The computational grid has been setup as a 2D spherical grid ( $r, \theta$ ). A logarithmic grid is used with 256 bins in the  $r$ -direction and uniform grid spacing in the  $\theta$ -direction with 90 bins. The outflow is launched at  $r_0$  and the outer radial boundary is set to an absorbing boundary condition, at 300 kpc. With this setup, the outflow does not reach the outer boundary during the simulation time of 300 Myr. The system reaches steady state at smaller distances at earlier times than this. Both the inner and outer boundary in the  $\theta$ -direction have been set to reflective. The simulation domain covers a single hemisphere, with  $\theta$  ranging from 0 to  $\pi/2$ .

## 3 CR TRANSPORT MODEL

The transport of CRs through an outflow is described, in its conservative form, by the following equation,

$$\frac{\partial f}{\partial t} = \nabla \cdot (D \nabla f - \mathbf{v} f) + \frac{1}{p^2} \frac{\partial}{\partial p} \left[ (\nabla \cdot \mathbf{v}) \frac{p^3}{3} f \right] - \frac{f}{\tau_{\text{loss}}} + \frac{Q}{p^2} \quad (12)$$

where  $f = \frac{dN}{d^3x d^3p}$  is the CR phase space density and  $N$  is the number of particles.  $D$  is the spatial diffusion coefficient,  $v$  is the outflow velocity,  $p$  is the CR momentum,  $\tau_{\text{loss}}$  is the energy loss time scale for  $pp$  collisions and  $Q$  is the CR spectrum injected per unit time and per unit volume (see

section 3.2). The first term on the right hand side of Eq. (12) represents the spatial diffusion of CRs through the outflow depending on the turbulence and strength of the magnetic field (see section 3.1) and spatial advection which acts to suppress the CR flux. The second term represents momentum advection which moves the CRs to lower energies as they are transported in the expanding advective outflow. The fourth term is the CR loss rate which is the rate at which the CRs lose their energy. A hadronic CR experiences energy losses through inelastic  $pp$  collisions (Gabici et al. 2007) in the halo region with a loss time scale  $\tau_{\text{loss}} \approx 20$  Gyr, on a halo distance scale of 10 kpc.

For the results (see section 4.2), the CR number density,  $n_{\text{CR}}$ , will be presented instead of  $f$ . In order to determine  $n_{\text{CR}}$  from  $f$  which the transport equation provides, the momentum dependence of the phase space distribution is integrated out,

$$n_{\text{CR}} = \int_{p_{\text{min}}}^{p_{\text{max}}} 4\pi f p^2 dp = \int_{p_{\text{min}}}^{p_{\text{max}}} \frac{dN}{d^3x dp} dp. \quad (13)$$

Here  $p_{\text{min}} = 10$  GeV/ $c$  and  $p_{\text{max}} = 30$  GeV/ $c$  are the minimum and maximum momentum for the injected CRs for the results presented in section 4.2. This range has been chosen to coincide with one of the selected ranges by Ackermann et al. (2014) for the  $\gamma$ -ray observations of the Fermi bubbles.

## 3.1 Diffusion coefficient

The diffusion coefficient determines the distance that a CR, on average, can travel through ambient magnetic fields until its momentum vector has changed significantly ( $\sim 1$  rad. in angle). For the purpose of the calculations, a simple commonly used expression for the diffusion coefficient is adopted (Schlickeiser 1989; Jokipii 1966), which expressed as a length-scale is,

$$\frac{D}{c} = 0.1 \left( \frac{p}{10 \text{ GeV}/c} \right)^{2-\gamma} \text{ pc}, \quad (14)$$

where  $c$  is the speed of light and  $\gamma = 5/3$  is the Kolmogorov turbulence power-spectrum slope.

## 3.2 Injection and CR spectrum

The injection site for the CR source is assumed to be at the base of the outflow at  $r_0$ . The volumetric injection rate  $Q$  is defined as,

$$Q = \frac{d\dot{N}}{d^3x dp}, \quad (15)$$

where  $\dot{N}$  is the number of particles injected per unit time.

A continuous injection spectrum has been used such that  $\frac{d\dot{N}}{dp} \propto p^{-\alpha} \exp(-p/p_{\text{max}})$ , with  $\alpha = 2$  representative of diffusive shock acceleration (Bell 1978), and  $p_{\text{max}} = 10^7$  GeV/ $c$ . The total injected luminosity is expressed as

$$L_{\text{CR}} = c \int_{p_{\text{min}}}^{p_{\text{max}}} p \frac{d\dot{N}}{dp} dp, \quad (16)$$

The total injected luminosity has been set to  $L_{\text{CR}} = 6 \times 10^{39} \text{ erg s}^{-1}$  which determines the value of  $\dot{N}$ . This value

has been chosen to match with the fitting range for the energy flux provided by the observations of the Fermi bubbles (Ackermann et al. 2014).

### 3.3 Numerical setup

Based on a 2D differencing scheme (Rodgers-Lee et al. 2017, 2020), the temporal evolution of  $f$ , using a steady-state subsonic velocity solution for the advection terms, is obtained for a timescale of 300 Myr. This timescale corresponds to the time needed to reach a steady-state out to 20 kpc, the spatial region of interest in this work. The grid adopted in these calculations has a cylindrical ( $R, z$ ) geometry with logarithmic spacing for both  $R$  and  $z$  grids with 350 bins. The outflow velocity,  $v$ , obtained from the hydrodynamic simulations (see section 2) has been used as an input for Eq. (12). Considering this velocity profile (see section 2.4) the inner boundary has been setup at 300 pc, and the outer boundary at 100 kpc. The CRs are injected close to the inner boundary. The momentum grid is logarithmically spaced with 5 bins ranging from 10 – 30 GeV/ $c$ . The simulations have been performed for one quadrant only. The results presented here have subsequently been reflected into the other quadrants.

## 4 RESULTS

### 4.1 Hydrodynamic outflow

Fig. 2 shows the 2D velocity profile of the subsonic outflow in both the  $R$  and  $z$ -directions. The Galactic potential adopted in this paper (see section 2.1), in combination with a temperature of  $kT \approx 400$  eV for the halo region, give two roots for Eq. (10). The velocity profile along the  $z$ -axis is shown in Fig. B1. Once injected at the inner radius (0.3 kpc) the gas first decelerates until reaching a distance of  $\sim 0.45$  kpc (see Appendix B) and then accelerates. This acceleration continues outwards up to  $r_c \approx 1$  kpc (red region in Fig. 2), reaching a velocity of  $v \approx 210$  km s $^{-1}$ , after which the gas then decelerates continuously (as shown by the orange to blue regions in Fig. 2). The outflow spreads mainly along the  $z$ -direction due to the asphericity of the disc component of the Galactic potential, see section 2.2. Near the Galactic center, the outflow takes a conic shape and extends progressively to a lobular shape as the outflow decelerates. It is found that the centrifugal force due to Galactic rotation has only a minor effect on the results. It reduces the gravitational force acting on the outflow at larger distances from the rotation axis slightly and mildly enhances the extension of the outflow velocity in the  $R$  direction. The continuous deceleration beyond  $r_c$ , along increasing Galactic latitude, gives the following velocities:  $v(z = 3$  kpc)  $\approx 120$  km s $^{-1}$ ,  $v(z = 5$  kpc)  $\approx 85$  km s $^{-1}$ ,  $v(z = 7$  kpc)  $\approx 70$  km s $^{-1}$  and  $v(z = 10$  kpc)  $\approx 53$  km s $^{-1}$ . These results appear compatible with observations of UV absorption lines of OI, AlII, CII, CIV, SiII, SiIII, SiIV and other species provided by Bordoloi et al. (2017) for the Local Standard of Rest velocity. However, the velocities given above are lower than the values inferred from similar UV absorption line studies (Karim et al. 2018) for the South Fermi bubbles. It should be noted that an asymmetry between the North and South Fermi lobes exists, potentially related to different density distributions in the two hemispheres (Sarkar 2019).

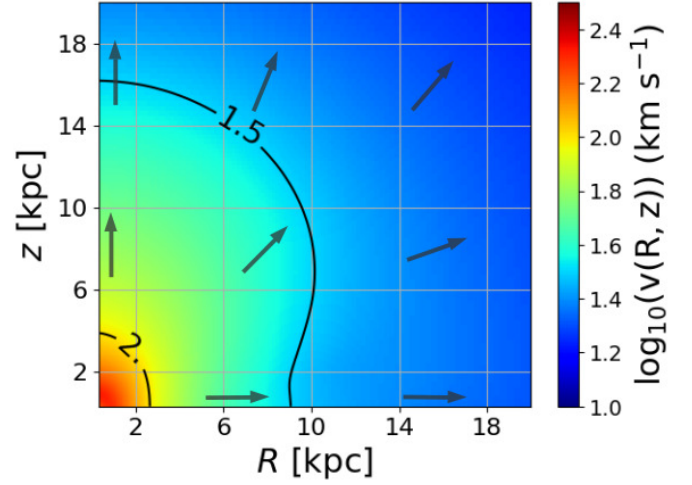


**Figure 2.** 2D spatial distribution of the subsonic velocity profile through a gravitational potential composed of a bulge, disc and halo with  $c_s \approx 250$  km s $^{-1}$ . The arrows represent the direction of propagation of the outflow. The continuous colourbar indicates the logarithm (base 10) of the magnitude of the velocity.

More recent observational results for both North and South Fermi lobes provided by Ashley et al. (2020) give a outflow profile similar to Karim et al. (2018) but with a somewhat faster velocity, by a factor  $\sim 10$ .

### 4.2 CR density map

Here the results related to the CR propagation through the outflow velocity region described in section 4.1 are presented. Advection and diffusion are the two terms in the transport equation (Eq. (12)) which compete to dictate the resultant CR transport. The diffusion mechanism can be ignored if the outflow velocity is high enough, and one is considering low energy ( $< 10$  GeV) CRs (see Eq. 14). However for the case of a Galactic breeze,  $v$  is sufficiently small such that both terms play an important role in dictating the resultant CR spatial distribution. This effect can be seen in Fig. 3, which shows a 2D plot of the CR number density distribution in the Galaxy produced with the model. In the vicinity of the GC, where the outflow velocity is the highest (as shown in by the red to blue-green region in Fig. 3), advection is the dominant transport mechanism. In this region, due to the asymmetry of the Galactic potential, the CRs propagate mainly along the  $z$ -direction. The velocity difference in the  $R$  and  $z$ -direction is less pronounced as the outflow decelerates. Subsequently, the bubble-shape becomes more spherical in shape at higher latitudes.

### 4.3 Gamma-ray emission map

Inelastic CR collisions with ambient gas in the Galactic halo results in the creation of charged and neutral pions. The dominant decay mode for neutral pions is into two photons (Particle Data Group et al. 2020). A photon produced by such a collision obtains  $\sim 10$  % of the initial CR proton energy. Therefore, for the 10-30 GeV CR energy range considered, photons with energy  $E_\gamma = 1 - 3$  GeV are produced. The total

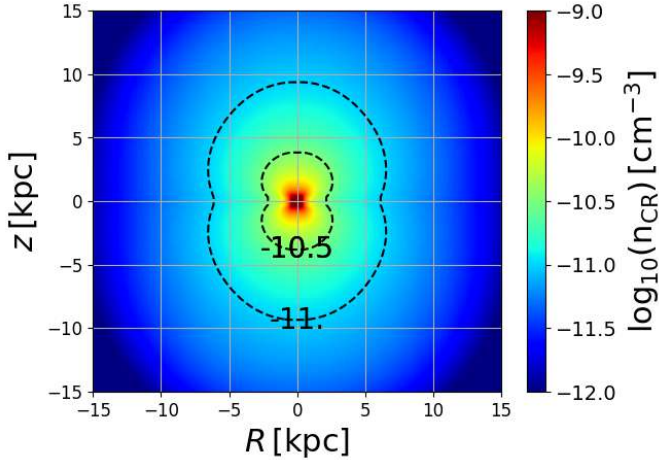


**Figure 3.** 2D CR spatial density distribution in the Galaxy for a energy range of  $E_{\text{CR}} = 10\text{--}30$  GeV. The dashed black lines are contours representing different density distribution. The continuous colourbar indicates the logarithm (base 10) of the cosmic ray density.

resulting gamma-ray brightness,  $E_\gamma F_\gamma$ , seen by an observer along a particular solid angle of angular size  $\Delta\Omega$  is obtained from summing the contribution over the full line-of-sight,

$$E_\gamma F_\gamma = \frac{1}{3\Delta\Omega} \int \frac{dL_\gamma}{4\pi r_{\text{obs}}^2} = \frac{1}{12\pi\tau_{\text{loss}}} \int e_{\text{CR}} dr_{\text{obs}}, \quad (17)$$

where  $r_{\text{obs}}$  is the distance between the source of emission and the observer. The factor of  $\frac{1}{3}$  in the above expression accounts for the fraction of neutral pions produced in inelastic CR collisions with the target gas. These neutral pions,  $\pi^0$ , subsequently quickly decay to gamma-ray photons, whereas the other two charged pions,  $\pi^+$  and  $\pi^-$ , also produced do not decay directly into gamma-ray photons. The position of the observer from the GC has been fixed at 8 kpc (Gillessen et al. 2017). The CR energy density,  $e_{\text{CR}}$  is expressed as

$$e_{\text{CR}} = \int_{p_{\text{min}}}^{p_{\text{max}}} 4\pi f p^3 dp. \quad (18)$$

The energy flux from all of the cells contained along the line-of-sight within each solid angle direction is summed up. The skymap of the gamma-ray energy flux density is shown in Fig. 4a for  $E_\gamma = 1\text{--}3$  GeV (Fig. 4b is for  $E_\gamma = 1\text{--}3$  TeV, see section 4.3.1). The simulated subsonic velocity profile in combination with  $L_{\text{CR}} = 6 \times 10^{39}$  erg s $^{-1}$  produces bilobal gamma-ray emission, with a pronounced pinch at low Galactic latitudes. From observations, the height of the Fermi bubbles is  $\sim 10$  kpc, corresponding to  $\sim 50^\circ$  for an observer at  $\sim 8$  kpc. For the gamma-ray energy range,  $E_\gamma = 1\text{--}3$  GeV produced with a subsonic outflow, the total gamma-ray luminosity is  $L_\gamma \approx 7 \times 10^{36}$  erg s $^{-1}$ . In comparison, observations indicate a gamma-ray luminosity, for an energy range from 0.1–500 GeV to be  $L_\gamma \approx 4.4 \times 10^{37}$  erg s $^{-1}$  (Ackermann et al. 2014), assuming a fixed emitting distance of 8 kpc. Adjusting their luminosity to our reduced energy range of 1–3 GeV, leads to  $L_\gamma \approx 7.5 \times 10^{36}$  erg s $^{-1}$ , which agrees well with the gamma-ray luminosity from our simulation.

The brightness of the gamma-ray energy flux produced appears broadly consistent with Fermi-LAT observations. How-

ever, the width of the observed Fermi bubbles, estimated to be around  $20^\circ$  from the central axis (Ackermann et al. 2014) are narrower than the simulation results shown here, which extend to a width of  $30^\circ$ . This difference originates from the assumptions in the adopted setup. Specifically, both the magnitude of the CR diffusion coefficient (see Eq. 12), and the isothermal gas temperature, collectively dictate the subsequent lobe width.

#### 4.3.1 Predictions for CTA and SWGO

The Cherenkov Telescope array (CTA, Acharya et al. 2018) and the Southern Wide-field gamma-ray Observatory (SWGO, Abreu et al. 2019), a wide field observatory that will complement CTA, are next generation ground-base gamma-ray instruments, which collectively will span an energy range from 20 GeV to 300 TeV (Abdalla et al. 2021). A simulation for the transport of  $E = 10\text{--}30$  TeV energy CRs has been run in order to predict what future observations of the Fermi bubbles will look like if a subsonic outflow is responsible for the gamma-ray emission. The gamma-ray emission map produced by the CRs is shown in Fig. 4b. These simulations are done with the same setup, for both the hydrodynamic outflow simulation (see Section 2.4) and the CR transport code (see Section 3.3).

Considering the adopted subsonic velocity profile and the high CR energies, diffusion plays a more prominent role (see Eq. (14)). Compared to the lower energy gamma-ray emission map shown in Fig. 4a, the gamma-ray distribution is wider and reaches a slightly lower height. This difference is due to the energy dependence of the diffusion coefficient adopted, which introduces energy dependent transport effects. For a latitude of  $\sim 50^\circ$  and a longitude of  $\sim 0^\circ$  the predicted energy flux observed, according to the subsonic model presented here, should be  $\sim 0.9 \times 10^{-8}$  GeV cm $^{-2}$  s $^{-1}$  sr $^{-1}$ .

Returning to the comparison between the Fermi-LAT data and Galactic breeze simulations results, in Fig. 5 a direct comparison is made between the simulations and data provided by the Fermi-LAT collaboration (Ackermann et al. 2014) for latitudes from  $b = 30^\circ\text{--}50^\circ$ . The blue line represents the energy flux provided by the simulations for a subsonic outflow. The red error bar ranges come from the data defined with the GALPROP CR propagation and interactions code (Vladimirov et al. 2011) as templates. The red shaded regions were computed from uncertainties of different models and different definitions of the templates. Both the red error bar ranges and the red shaded regions are from Ackermann et al. (2014). At latitudes between  $30^\circ < b < 40^\circ$  and  $40^\circ < b < 50^\circ$ , (for  $-15^\circ < l < 15^\circ$ ), the energy flux is broadly compatible with the observations, although as already noted previously, beyond a longitude of  $15^\circ$  the energy flux no longer falls within the red shaded region due to the broader width of the simulated lobes.

## 5 CONCLUSIONS AND OUTLOOK

Following on from an earlier investigation (Taylor & Giacinti 2017) into a subsonic outflow origin for the Fermi bubbles, a hydrodynamical outflow simulation has been carried out

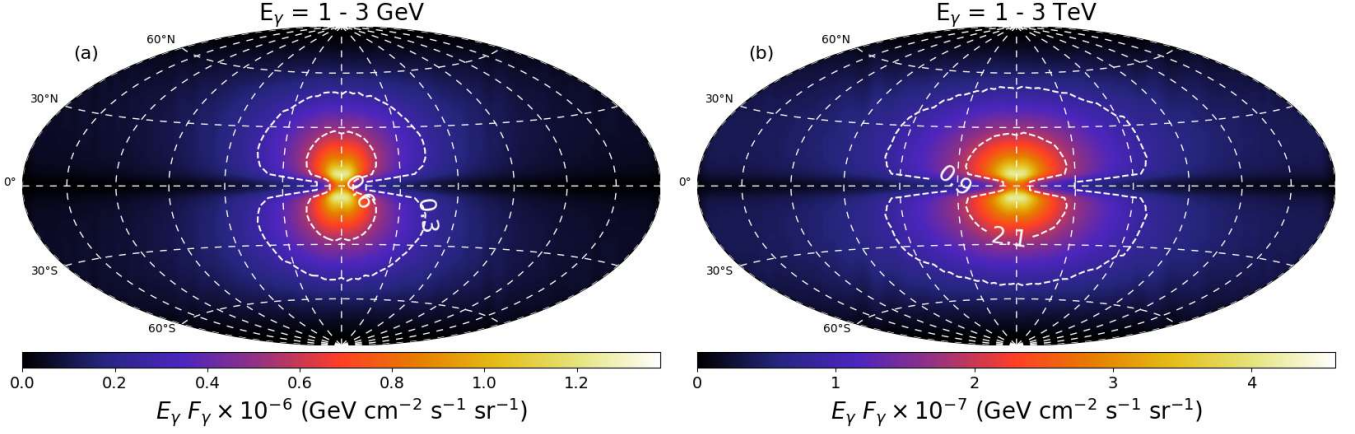


**Figure 4.**  $\gamma$ -ray emission maps produced with a subsonic outflow. **Left:** The emission is produced by photons with energy ranging from 1 to 3 GeV. **Right:** The emission is produced by photons with energy ranging from 1 to 3 TeV. It is important to note that colour bar limits are not the same for the two plots.

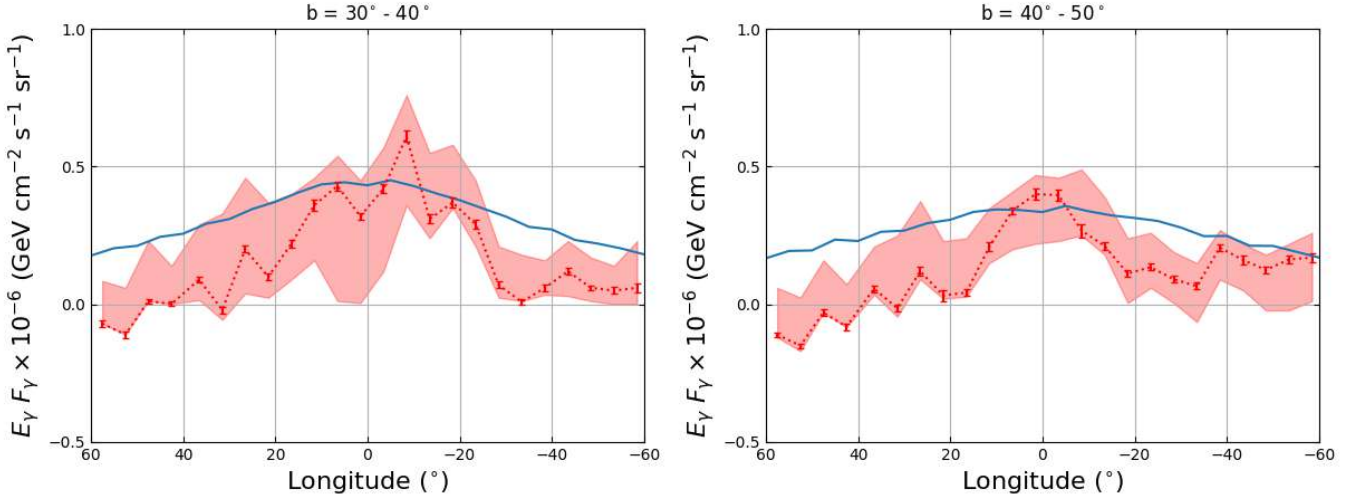


**Figure 5.** The photon energy flux produced by the gamma-ray emission is plotted as a function of Galactic longitude for different latitude ranges. The blue line represent the energy flux provided by the simulations for a subsonic outflow presented in this paper. The error bar ranges and the shaded red region are provided by the Fermi-LAT observational results (Ackermann et al. 2014). The red error bars represent the energy flux determined from observations of the Fermi bubbles. The shaded red region has been computed from uncertainties of different models and different possible templates. **Left:** The photon energy flux is compared with Fermi-LAT data for  $b = 30^\circ - 40^\circ$ . **Right:** The photon energy flux is compared with Fermi-LAT data for  $b = 40^\circ - 50^\circ$ .

here. The outflow velocity profile provided by the hydrodynamic simulation is then used as part of a 2D CR transport code description. CRs transported by the outflow into the Galactic halo region subsequently undergo inelastic  $pp$  energy loss interactions with the low density hot ambient gas present. These energy loss interactions give rise to spatially dependent gamma-ray emission. A comparison of this emission is made, for a specific photon energy range of 1–3 GeV, with Fermi bubbles observations data provided by the Fermi-LAT satellite. Following these results a higher energy emission map prediction is provided, in the 1–3 TeV energy range of relevance for next generation instruments (CTA/SWGO).

The hydrodynamic simulation results presented in this paper reveal that the Galactic breeze propagates predominantly in the direction orthogonal to the Galactic plane. This outflow subsequently develops a conical shape, which eventually

become lobe-like in shape at large distances. The continuous deceleration of the outflow beyond the critical radius appears consistent with UV absorption line observations of cold clouds within the Fermi bubbles region (Bordoloi et al. 2017; Ashley et al. 2020). Moreover, the Galactic breeze model does not sweep up the ambient Galactic density as winds do. The initial hydrostatic density distribution is instead largely preserved, motivating halo densities which appear consistent with observations provided for the Milky-Way (Gupta et al. 2017; Zhang & Guo 2021; Martynenko 2022). A comparison of the gamma-ray sky map emission produced by the CR energy losses show that these are broadly compatible with the Fermi bubbles observations provided by Ackermann et al. (2014). This compatibility obtained from a model with so few assumptions supports the proposal that a Galactic breeze provides a self-consistent description for the origin of the bub-

bles. However it is noted that further improvements to the model are motivated. Specifically, these improvements concern the adoption of a more complex temperature distribution and the inclusion of magnetic fields in the PLUTO simulation.

Fundamentally, the present limited knowledge about the nature of the Galactic halo region (ie. the gas density and temperature, and the shape of the Galactic potential) limits the ability to describe gas and CR transport through this region. Of particular additional concern are Galactic halo magnetic fields, which have not been considered explicitly in the transport description used here. However, these fields certainly play an intrinsic role in CR diffusion, and likely also play a role in a more complete magneto-hydrodynamic description of the gas outflow. Furthermore, the presence and strength of these magnetic fields may well underlie aspects of the Fermi bubbles morphology. For example, the bubbles edges observed in gamma-ray emission may relate to the magnetic field geometry in this region, hindering the diffusion of particles across the bubbles edges. This would provide a dimmer surface brightness at the bubbles edges.

Additional information about the Galactic halo magnetic fields have been provided by the WMAP Haze (Dobler & Finkbeiner 2008; Dobler 2012) and S-PASS bubble (Carretti et al. 2013). Both the WMAP Haze and S-PASS bubble appear spatially coincident with the base of the Fermi bubbles, although the haze appears to extend only up to  $\sim 6$  kpc in height. Within the Galactic breeze scenario, this synchrotron emission is produced by both primary electrons, and secondary electrons produced through pp interactions, with the former dominating at low Galactic latitudes. Future PLUTO simulations incorporating magnetic fields will allow this possibility to be explored.

The eROSITA soft X-ray bubbles also provides new insights about the Galactic halo environment. This emission is thought to originate from energetic thermal electrons, indicating that a heating mechanism for this gas is operating. Within the Galactic breeze thermally driven outflow model, this same heating mechanism is responsible for the hot isothermal gas temperature adopted. Potentially, the heating mechanism for the gas may be magnetic (Alfvén wave) heating. However, provided that a hot gas temperature is maintained, the driving mechanism for the heating of the gas is not of primary focus.

Further observations probing the nature of the halo environment are needed in order to provide a better constraint on the Galactic potential and temperature for the gas throughout the Galaxy. Observations of cold clouds in the Fermi bubbles, at 2–3 kpc from the GC, give a velocity outflow of  $\sim 330$  km s $^{-1}$  (Ashley et al. 2020). Such a value is hardly reachable for an isothermal subsonic description considering the fitting range for the Galactic gravitational potential provided by Watkins et al. (2019). On the other hand, the apparent continuous deceleration of the gas observed with increasing latitude (Bordoloi et al. 2017; Ashley et al. 2020), is compatible with a subsonic outflow scenario. A single temperature model, therefore, may provide an insufficiently accurate account of the gas velocity evolution. Indeed, evidence for a transition between a hot bulge and an even hotter halo ( $\sim 1$  keV) out at larger distances (Das et al. 2019a,b, 2021), motivates the consideration of a more complex temperature profile than the one considered here.

## ACKNOWLEDGEMENTS

The authors would like to thank the anonymous reviewer for their valuable comments which helped to improve the manuscript. OT and AMT acknowledge support from DESY (Zeuthen, Germany), a member of the Helmholtz Association HGF. DRL would like to acknowledge that this publication has emanated from research conducted with the financial support of Science Foundation Ireland under Grant number 21/PATH-S/9339.

## DATA AVAILABILITY

The data underlying this article will be shared on reasonable request to the corresponding author.

## REFERENCES

- Abdalla H., et al., 2021, *J. Cosmology Astropart. Phys.*, 2021, 048  
 Abreu P., et al., 2019, The Southern Wide-Field Gamma-Ray Observatory (SWG0): A Next-Generation Ground-Based Survey Instrument for VHE Gamma-Ray Astronomy. ([arXiv:1907.07737](https://arxiv.org/abs/1907.07737))  
 Acharya B. S., et al., 2018, Science with the Cherenkov Telescope Array. WSP ([arXiv:1709.07997](https://arxiv.org/abs/1709.07997)), doi:10.1142/10986  
 Ackermann M., et al., 2014, *ApJ*, 793, 64  
 Ashley T., Fox A. J., Jenkins E. B., Wakker B. P., Bordoloi R., Lockman F. J., Savage B. D., Karim T., 2020, *ApJ*, 898, 128  
 Bell A. R., 1978, *MNRAS*, 182, 147  
 Bhattacharjee P., Chaudhury S., Kundu S., 2014, *ApJ*, 785, 63  
 Bordoloi R., et al., 2017, *ApJ*, 834, 191  
 Burbidge E. M., Burbidge G. R., Rubin V. C., 1964, *ApJ*, 140, 942  
 Bustard C., Pardy S. A., D’Onghia E., Zweibel E. G., Gallagher J. S. I., 2018, *ApJ*, 863, 49  
 Carretti E., et al., 2013, *Nature*, 493, 66  
 Cashman F. H., et al., 2021, *ApJ*, 923, L11  
 Chamberlain J. W., 1965, *ApJ*, 141, 320  
 Chan T. K., Keres D., Gurvich A. B., Hopkins P., Trapp C., Ji S., Faucher-Giguere C.-A., 2021, arXiv e-prints, p. [arXiv:2110.06231](https://arxiv.org/abs/2110.06231)  
 Cheng L. X., et al., 1997, *ApJ*, 481, L43  
 Cheng K. S., Chernyshov D. O., Dogiel V. A., Ko C. M., Ip W. H., 2011, *ApJ*, 731, L17  
 Chevalier R. A., Clegg A. W., 1985, *Nature*, 317, 44  
 Crocker R. M., Aharonian F., 2011, *Phys. Rev. Lett.*, 106, 101102  
 Crocker R. M., Bicknell G. V., Taylor A. M., Carretti E., 2015, *ApJ*, 808, 107  
 Das S., Mathur S., Nicastro F., Krongold Y., 2019a, *ApJ*, 882, L23  
 Das S., Mathur S., Gupta A., Nicastro F., Krongold Y., 2019b, *ApJ*, 887, 257  
 Das S., Mathur S., Gupta A., Krongold Y., 2021, *ApJ*, 918, 83  
 Dobler G., 2012, *ApJ*, 750, 17  
 Dobler G., Finkbeiner D. P., 2008, *ApJ*, 680, 1222  
 Dobler G., Finkbeiner D. P., Cholis I., Slatyer T., Weiner N., 2010, *ApJ*, 717, 825  
 Everett J. E., Murray N., 2007, *ApJ*, 656, 93  
 Fichtner H., 1997, in International Cosmic Ray Conference. p. 397  
 Finkbeiner D. P., 2004, *ApJ*, 614, 186  
 Flynn C., Sommer-Larsen J., Christensen P. R., 1996, *MNRAS*, 281, 1027  
 Fox A. J., et al., 2015, *ApJ*, 799, L7  
 Gabici S., Aharonian F. A., Blasi P., 2007, *Ap&SS*, 309, 365  
 Gaia Collaboration et al., 2016a, *A&A*, 595, A1  
 Gaia Collaboration et al., 2016b, *A&A*, 595, A2  
 Gaia Collaboration et al., 2018, *A&A*, 616, A1



Gillessen S., et al., 2017, *ApJ*, **837**, 30

Guo F., 2017, The AGN Jet Model of the Fermi Bubbles. pp 189–192 ([arXiv:1609.07705](https://arxiv.org/abs/1609.07705)), doi:10.1017/S1743921316012023

Guo F., Mathews W. G., 2012, *ApJ*, **756**, 181

Gupta A., Mathur S., Krongold Y., 2017, *ApJ*, **836**, 243

Holzer T. E., Axford W. I., 1970, *ARA&A*, **8**, 31

Igarashi A., Mori M., Nitta S.-y., 2014, *MNRAS*, **444**, 1177

Igarashi A., Mori M., Nitta S.-y., 2017, *MNRAS*, **470**, 2225

Jokipii J. R., 1966, *ApJ*, **146**, 480

Karim T., et al., 2018, *ApJ*, **860**, 98

Lamers H. J. G. L. M., Cassinelli J. P., 1999, Basic concepts: isothermal winds. Cambridge University Press, p. 60–91, doi:10.1017/CBO9781139175012.004

Lockman F. J., 1984, *ApJ*, **283**, 90

Lockman F. J., Di Teodoro E. M., McClure-Griffiths N. M., 2020, *ApJ*, **888**, 51

Lynds C. R., Sandage A. R., 1963, *ApJ*, **137**, 1005

Martynenko N., 2022, *MNRAS*, **511**, 843

Mathews W. G., Baker J. C., 1971, *ApJ*, **170**, 241

Mertsch P., Petrosian V., 2019, *A&A*, **622**, A203

Mignone A., Bodo G., Massaglia S., Matsakos T., Tesileanu O., Zanni C., Ferrari A., 2007, *ApJ*, **170**, 228–242

Miyamoto M., Nagai R., 1975, *PASJ*, **27**, 533

Morris M., Serabyn E., 1996, *ARA&A*, **34**, 645

Mou G., Yuan F., Bu D., Sun M., Su M., 2014, *ApJ*, **790**, 109

Mou G., Yuan F., Gan Z., Sun M., 2015, *ApJ*, **811**, 37

Navarro J. F., Frenk C. S., White S. D. M., 1996, *ApJ*, **462**, 563

Parker E. N., 1958, *ApJ*, **128**, 664

Parker E. N., 1965, *ApJ*, **141**, 1463

Particle Data Group et al., 2020, *Progress of Theoretical and Experimental Physics*, **2020**, 083C01

Planck Collaboration et al., 2013, *A&A*, **554**, A139

Predehl P., et al., 2020, *Nature*, **588**, 227

Rodgers-Lee D., Taylor A. M., Ray T. P., Downes T. P., 2017, *MNRAS*, **472**, 26

Rodgers-Lee D., Vidotto A. A., Taylor A. M., Rimmer P. B., Downes T. P., 2020, *MNRAS*, **499**, 2124

Sarkar K. C., 2019, *MNRAS*, **482**, 4813

Sarkar K. C., Nath B. B., Sharma P., 2017, *MNRAS*, **467**, 3544

Schlickeiser R., 1989, *ApJ*, **336**, 243

Sofue Y., 2013, *PASJ*, **65**, 118

Sofue Y., 2022, *PASJ*,

Songaila A., 1997, *ApJ*, **490**, L1

Su M., Slatyer T. R., Finkbeiner D. P., 2010, *ApJ*, **724**, 1044

Taylor A. M., Giacinti G., 2017, *Phys. Rev. D*, **95**, 023001

Taylor C., Boylan-Kolchin M., Torrey P., Vogelsberger M., Hernquist L., 2016, *MNRAS*, **461**, 3483

Tsuchiya M., Mori M., Nitta S.-y., 2013, *MNRAS*, **432**, 2837

Tumlinson J., Peebles M. S., Werk J. K., 2017, *ARA&A*, **55**, 389

Vladimirov A. E., et al., 2011, *Computer Physics Communications*, **182**, 1156

Watkins L. L., van der Marel R. P., Sohn S. T., Evans N. W., 2019, *ApJ*, **873**, 118

Yang H. Y. K., Ruszkowski M., 2017, *ApJ*, **850**, 2

Yang H. Y. K., Ruszkowski M., Ricker P. M., Zweibel E., Lee D., 2012, *ApJ*, **761**, 185

Yang H. Y. K., Ruszkowski M., Zweibel E., 2013, *MNRAS*, **436**, 2734

Yang H. Y., Ruszkowski M., Zweibel E., 2018, *Galaxies*, **6**, 29

Zhang R., Guo F., 2021, *ApJ*, **915**, 85

de Avillez M., Breitschwerdt D., 2004, *Ap&SS*, **292**, 207

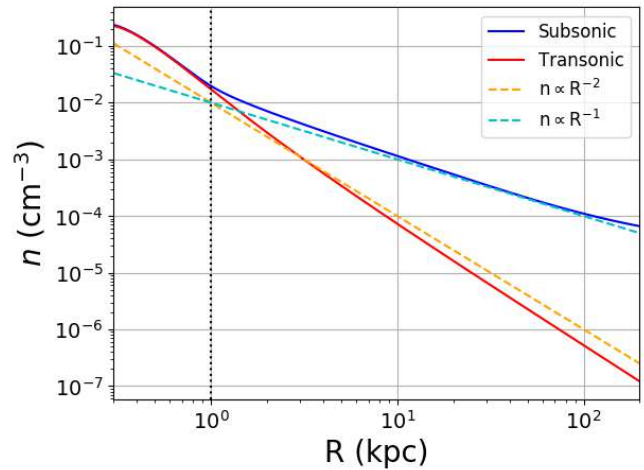


**Figure A1.** Two density distributions for two specific solutions for the outflow, namely subsonic and transonic. A subsonic solution (solid blue line) leads to a rather flat density distribution, similar to the initial hydrostatic density distribution. This distribution can be approximated by a power-law distribution,  $n \sim R^{-1}$  (cyan dashed line). A transonic solution (solid red line) produces a steeply falling density distribution beyond the critical radius (black vertical dotted line). This distribution can be approximated by the following power-law distribution,  $n \sim R^{-2}$  (orange dashed line).

## APPENDIX A: HYDROSTATIC DENSITY DISTRIBUTION AND INFLUENCE OF THE OUTFLOW

Fig. A1 shows the density distributions for the subsonic and transonic outflow cases. For the subsonic outflow (blue line), the density distribution is approximately the same as that for the hydrostatic case (defined by Eq. 11), whereas the density distribution is changed significantly under the influence of a transonic outflow (red line). It is noted that the initial hydrostatic density distribution is compatible, in the 10–100 kpc distance range, with the constraints from the ram pressure stripping of satellite galaxies around the Milky Way (Martynenko 2022).

## APPENDIX B: COMPARISON OF THE GALACTIC BREEZE WITH OBSERVATIONS

In Fig. B1 the Galactic breeze produced by the hydrodynamical simulation is presented. As explained in section 4.1, the velocity values for the simulated outflow are too low when compared with observations. Around 1 kpc, the Galactic breeze has a velocity of  $\sim 215 \text{ km s}^{-1}$  where the observations seem to suggest  $\sim 300 \text{ km s}^{-1}$ . However the deceleration of a subsonic outflow profile is still present and seems to match well with the deceleration observed in the North and South Fermi lobes (Bordoloi et al. 2017; Ashley et al. 2020).

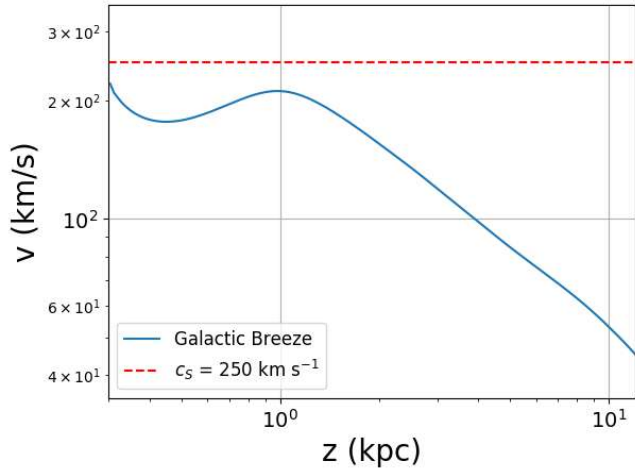


**Figure B1.** The velocity distribution produced by a Galactic breeze (solid blue line) is plotted along the  $z$ -axis (at  $R = 0.3$  kpc). The gravitational potential used in this work dictates the behaviour of the outflow. It reaches a maximum at the critical radius (1 kpc) and then decelerates continuously. The dashed red line corresponds to the thermal velocity,  $c_s$ , for the isothermal gas considered in this paper.